# Wide-field coherent anti-Stokes Raman scattering microscopy using random illuminations

Eric Fantuzzi, Sandro Heuke, Simon Labouesse, Dominykas Gudavičius, Randy Bartels, Anne Sentenac, Hervé Rigneault

# Wide-field coherent anti-Stokes Raman scattering microscopy using random illuminations (CARS-RIM)

ERIC M. FANTUZZI[1,†], SANDRO HEUKE[1,†], SIMON LABOUESSE[2], DOMINYKAS GUDAVIČIUS[3,4], RANDY BARTELS[5,6,7], ANNE SENTENAC[1,*] AND HERVÉ RIGNEAULT[1,*]

[1]*Aix Marseille Univ, CNRS, Centrale Marseille, Turing Center for Living Systems, Institut Fresnel, Marseille, France.*
[2]*Toulouse Université, CNRS, Centre de Biologie Intégrative, Toulouse, France*
[3]*Light Conversion, Keramiku st. 2B, LT-10233 Vilnius, Lithuania*
[4]*Cardiff University, School of Physics and Astronomy, The Parade, Cardiff CF24 3AA, United Kingdom.*
[5]*Colorado State University, Fort Collins, USA.*
[6]*Morgridge Institute for Research, Madison, WI USA USA.*
[7]*Department of Biomedical Engineering, University of Wisconsin, Madison Madison, WI USA.*
[†]*Contributed equally.*
[*]*Corresponding authors: anne.sentenac@fresnel.fr, herve.rigneault@fresnel.fr*

**Abstract: Coherent Raman microscopy is the method of choice for label-free, real-time characterization of the chemical composition in biomedical samples. The common implementation relies on scanning two tightly focused laser beams across the sample, which frequently leads to sample damage and proves slow over large fields of view. The few existing wide-field techniques for their part, feature a reduced lateral resolution and do not provide axial sectioning. To solve these practical limitations, we developed a robust wide-field nonlinear microscope that combines Random Illumination Microscopy (RIM) with coherent anti-Stokes Raman scattering (CARS) and sum frequency generation (SFG) contrasts. Based on a comprehensive theoretical study, CARS-RIM provides super-resolved reconstructions and optical sectioning of the sample from the second-order statistics of multiple images obtained under different speckled illuminations. We experimentally show that multimodal CARS-RIM and SFG-RIM achieve wide-field nonlinear imaging with a 3 micron axial sectioning capability and a 300 nm transverse resolution, while effectively reducing the peak intensity at the sample compared to conventional point scanning CARS. We exemplify the label free, highly contrasted, chemical imaging potential of CARS-RIM and SFG-RIM wide-field microscopy in 2D, as well as 3D, for a variety of samples such as beads, unstained human breast tissue, and a mixture of chemical compounds.**

## 1. Introduction

Tissue and cell imaging heavily relies on the use of chemical markers, fluorescent probes or dyes, to reveal different chemical species like DNA, proteins, or lipids. These staining techniques are time consuming, may cause unwanted perturbations of the samples and are not adapted to situations where markers cannot be used such as in some medical applications. Conversely, label free microscopy techniques, such as coherent anti-Stokes Raman scattering (CARS), offer chemical sensitivity, intrinsic 3D sampling, and real-time imaging within a limited field of view. CARS is a spectroscopic technique based on a nonlinear four-wave mixing process that is sensitive to the vibrational levels of chemical bonds [1]. In point scanning CARS microscopy [2], the sample is illuminated by two high power laser beams (the pump and the Stokes) that are scanned across the sample to produce an image from the CARS scattered power. Molecular-specific image structure is obtained when the pump and Stokes frequency difference matches the frequency of vibration of a given molecule. At this condition, the nonlinear light-matter interaction becomes

resonant within the targeted chemical bond and results in a surge of coherent radiation at a third frequency (the anti-Stokes light) [3]. Because CARS detects molecular signatures without requiring the introduction of labels, it has been extensively used for imaging of biochemical constituents in a variety of samples ranging from material science to biology and medicine [4]. CARS microscopy implemented with focused NIR beams provides good penetration in water, high lateral resolution (~300 nm) [2], and optical sectioning of ~ few microns. This explains its growing success for chemical imaging of fixed or living biological samples [5–7] and more recently for histological applications [8].

In practice, CARS imaging is performed by scanning the sample with the superposition of tightly focused pump and Stokes beams and the anti-Stokes light is collected with a light sensitive detector, such as a photomultiplier tube. Signal is collected from each focus point in the sample for long enough dwell time to reach a useful image quality. Speeding up the scanning process, to cover large regions or for *in vivo* studies, requires the diminution of the detector integration time per focus point and therefore leads to the inevitable increase of the laser powers to compensate for the loss of anti-Stokes signal. Working at few images per second over few hundred microns field of view requires tens to hundreds of milliwatts focused onto diffraction limited spots [5]. These power levels are often above the photo-induced sample damage threshold [9], which limits the illumination power and drastically restricts the scope of applications of rapid point scanning CARS imaging.

To reduce the photo-toxicity, the excitation power can be dispersed over a large area of the sample and then image the anti-Stokes light onto a camera. In this wide-field scheme, the necessary long integration time is compensated by the simultaneous acquisition of the signal on the multiple camera pixels. Several wide-field CARS microscopes were developed in which the sample was illuminated by collimated pump and Stokes laser beams, either in a collinear or folded-box geometry [10–13]. These schemes, however, introduced new difficulties. First, the collimated illuminations at the sample plane lead to focused beams at the objective back-focal plane, a situation that is likely to damage the optics when using high-peak laser power - see Fig. 1a. Second, wide-field CARS does not provide the optical sectioning and transverse resolution of point scanning CARS.

In this context, speckled illuminations, obtained by scattering coherent light with a diffuser, seem ideally suited for replacing the collimated beams in a wide-field imaging configuration. Speckles can be viewed as a multitude of randomly placed focused spots that probe the sample in parallel, and that are suitable for achieving high resolution due to their wide spread in spatial-frequency space. As the beam intensity is simultaneously spread across a large area in both the spatial and spatial frequency domains, the power of the laser beams can be increased without damaging the sample or the optics – a necessity for scaling the field of view. In this work, we developed a wide-field CARS microscope that combines speckled illuminations with the principles of random illumination microscopy (RIM) for precise computation of the sample density. We show that random illumination CARS microscopy (CARS-RIM) achieves molecular specificity with axial and transverse resolutions comparable to that of scanning-CARS, but obtained in a wide-field configuration with reduced illumination peak intensity.

## 2. Theory of CARS-RIM

RIM was initially developed as a super-resolved wide-field fluorescence imaging technique in which multiple images of a fluorescent sample are recorded under different random speckled illuminations. A super-resolved image of the sample is recovered numerically from the variance of the speckled images using a variance matching procedure based on the knowledge of the speckle auto-correlation. It was shown that the RIM image processing doubles the transverse resolution and provides an axial resolution comparable to that of an ideal confocal fluorescence microscope [14–16]. The RIM concept was developed for incoherent imaging systems in which

the intensity recorded by the camera can be modeled as the sum of the intensities emitted by each point-source of the sample. In particular, when the speckled illuminations are changed, the bright spots corresponding to in-focus object planes show larger signal variations than the larger blurred spots coming from out-of-focus object planes, Fig. 1c. However, CARS is a coherent scattering process. The recorded image is a complex interference pattern of the fields radiated by all the nonlinear induced CARS dipoles and there is no distinction between the out and in-focus sources, Fig. 1b. Transferring the principles of RIM to coherent nonlinear microscopy is, therefore, not straightforward.

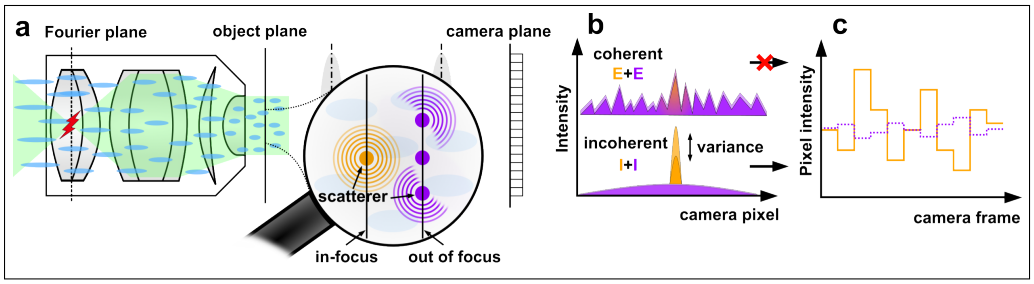


Fig. 1. Challenges in nonlinear wide-field microscopy: a) a high power plane-wave illumination (in green) easily damages the objective lens while a wide-field speckled illumination (in blue) avoids focusing at any plane. b) In coherent imaging, interference between the coherent radiation arising from scatterers placed at different object planes (orange and purple) leads to a pronounced signal variation in the image camera plane. In incoherent imaging, the intensities stemming from the different sources are summed. The light coming from out of focus sources forms blurred spots at the camera plane and contributes less to the overall image variance. c) Optical sectioning in incoherent imaging using the variance of speckled images: when illuminated with varying speckle intensities, the image from in-focus scatterers (orange) leads to a larger frame to frame intensity variation (large standard deviation) than that of out of focus scatterers (purple).

In the following, we show how it is possible to take advantage of the independence between the random speckled pump and Stokes beams involved in the CARS process to generate a "quasi-incoherent" CARS emission. The idea is to vary rapidly the pump speckle while the Stokes speckle is kept static such that each CARS active speckle grain, generated by the superposition of pump and Stokes speckle grains, acquire a randomly and rapidly varying phase (due to the rapidly changing pump speckle). If the resulting CARS speckle grain phase variation is fast compared to the camera integration time, one expects the recorded CARS radiation to have some similarity with the light stemming from incoherent sources. More precisely, the phase of two CARS scatterers is fully random as soon as they are displaced from each other by more than the square of the speckle pump grain. This combination was proposed more then ten years ago by Heinrich *et al* [17] but in absence of theoretical grounds and of satisfactory results, the approach was abandoned. In this work, we developed the theory of CARS imaging under speckled illuminations. In brief, we modeled the CARS image obtained under fixed pump and Stokes illuminations and derived its expression when the pump speckles are varied during the camera integration time. Then, we studied the conditions under which this expression resembles the fluorescence image model.

We consider a transmission microscope similar to the one presented schematically in Figs. 2a and 3. The sample is defined by its nonlinear susceptibility $\chi^{(3)}_{aS}$ and is illuminated by two co-propagating, fully developed, pump and Stokes speckled fields, $E_p$ and $E_S$ passing through condensers with numerical apertures $\mathrm{NA_S}$ and $\mathrm{NA_p}$. For simplification, the susceptibility tensor and the excitation fields are assumed to be scalar. The pump and Stokes fields are

modeled as random complex variables of zero mean and known correlation functions which depend on the numerical aperture of the illumination condenser objectives [18], $C_{p,S}(\mathbf{r_1}-\mathbf{r}_2) = \langle E_{p,S}(\mathbf{r}_1)E^*_{p,S}(\mathbf{r}_2)\rangle$, where $\langle\cdot\rangle$ stands for the averaging over different realizations of the speckles. The CARS emitted field, $E_{aS}$, is collected in the forward direction, through an objective of numerical aperture $\mathrm{NA_{aS}}$ and a tube lens, onto a camera. The CARS intensity, $I_{aS}$, at the pixel $\mathbf{R}$ of the image plane reads [19],

$$I_{aS}(\mathbf{R}) = |E_{aS}|^2(\mathbf{R}) = \left|\iiint G_{aS}(\mathbf{R},\mathbf{r})\chi^{(3)}_{aS}(\mathbf{r})E^2_p(\mathbf{r})E^*_S(\mathbf{r})\mathrm{d}\mathbf{r}\right|^2, \tag{1}$$

where $G_{aS}(\mathbf{R},\mathbf{r})$ is the anti-Stokes Green function that describes propagation of the anti-Stokes field, with wavelength $\lambda_{aS}$, that is radiated from a point source located at $\mathbf{r}$ in the sample and propagates to a point $\mathbf{R}$ in the image plane. Note that the Fourier supports of $G_{aS}$, $E_p$ and $E_S$ are all caps of sphere defined by their radius $1/\lambda_{aS,S,p}$, with their projection onto the transverse $(x,y)$ plane disks of radius $\mathrm{NA_{aS,S,p}}/\lambda_{\mathrm{aS,S,p}}$. Also, the Fourier supports of $C_p$ and $C_S$ are the same as that of $E_p$ and $E_S$ (see the supplemental information 1 part 1).

As the pump and Stokes speckled beams are formed independently, by choosing a suitably long camera integration time, it is possible to record the average of $I_{aS}$ over many realizations of the pump speckled field, while the Stokes field is kept constant. The intensity averaged over the pump speckles (denoted as $\langle\cdot\rangle_{\mathrm{p}}$) reads,

$$\langle I_{aS}\rangle_{\mathrm{p}}(\mathbf{R}) = \iiint\iiint G_{aS}(\mathbf{R},\mathbf{r}_1)\chi^{(3)}_{aS}(\mathbf{r}_1)E^*_S(\mathbf{r}_1)G^*_{aS}(\mathbf{R},\mathbf{r}_2)\chi^{(3)*}_{aS}(\mathbf{r}_2)\,\langle E^2_p(\mathbf{r}_1)E^{2*}_p(\mathbf{r}_2)\rangle\, E_S(\mathbf{r}_2)\mathrm{d}\mathbf{r}_1\mathrm{d}\mathbf{r}_2, \tag{2}$$

where $a^*$ stands for the conjugate of $a$ and $\langle E^2_p(\mathbf{r}_1)E^{2*}_p(\mathbf{r}_2)\rangle$, the characteristic function of the pump speckle grain, is equal to $2C^2_p(\mathbf{r}_1-\mathbf{r}_2)$ [18]. Hereafter, the pump averaged image $\langle I_{aS}\rangle_{\mathrm{p}}$ will be called a speckle-CARS image. It corresponds to the image that is recorded on the camera when the Stokes speckled illumination is static and the pump speckles vary rapidly during the integration time.

If the sample is made of isolated point-like scatterers that are separated by more than the width of $C^2_p$, Eq. (2) can be simplified to,

$$\langle I_{aS}\rangle_{\mathrm{p}}(\mathbf{R}) = I_{aS}(\mathbf{R}) = 2I^2_p\iiint |G_{aS}|^2(\mathbf{R},\mathbf{r})|\chi^{(3)}_{aS}|^2(\mathbf{r})|E_S|^2(\mathbf{r})\mathrm{d}\mathbf{r}. \tag{3}$$

Equation (3) corresponds to the model of a fluorescence image obtained under a speckled illumination which is used in RIM [14, 16], $g_{aS} = |G_{aS}|^2$ is the standard fluorescence point spread function at emission wavelength $\lambda_{aS}$, $|E_S|^2$ is the speckle intensity for each static Stokes speckle illumination, and $|\chi^{(3)}_{aS}|^2$ is analogous to the fluorescence density. This result can be understood by noting that each CARS point-scatterer is tagged by the uncorrelated random phases of the pump field so that, when averaging over many pump speckled illuminations, the field emitted by each CARS source add in intensity on the camera in the same way as that of fluorophores. Yet, this result implicitly requires the sample to be sparse. Interestingly, and less restrictively, we show in the supplementary information 1 part 1 that the same fluorescence-like model can be obtained if $\chi^{(3)}_{aS}$ varies slowly in space over the width of $C^2_p$. In this case, $g_{aS}$ is slightly different and accounts for the coherent radiation of the CARS sources over the pump speckle excitation grains.

Following the RIM approach, CARS-RIM requires the recording of multiple speckle-CARS images for different Stokes speckled illuminations. A first estimate of the sample, hereafter called

average-CARS, can be obtained by simply averaging these speckle-CARS images. Note that the averaging can be implemented experimentally by simultaneously varying both the Stokes and pump speckles during the camera integration time. Recalling that $\langle |E_S|^2 \rangle$ , is constant throughout the field of view, average-CARS $\langle \langle I_{aS} \rangle_{\mathrm{p}} \rangle_S$, is similar to the image provided by a fluorescence microscope using homogeneous illumination. The average-CARS image follows the model of incoherent wide-field imaging, which is proportional to the sample density (here $|\chi^{(3)}_{aS}|^2$) convolved with $g_{aS}$. Because of the missing cone of the Fourier support of $g_{aS}$, average-CARS does not provide optical sectioning. Yet, its resolution is expected to be better than that of widefield 'coherent' microscopes using collimated laser beams (assimilated to plane waves). Indeed, in coherent imaging, the image, given by the square of Eq. (1), is related to the sample convolved with $G_{aS}$ which has a significantly larger footprint than $g_{aS} = |G_{aS}|^2$ and explains the poor lateral resolution of the existing widefield CARS microscopes.

In the RIM technique, the sample is not reconstructed from the average of the speckled images but from their variance [16]. In CARS-RIM, the variance of the speckle-CARS images reads,

$$\mathcal{V}[(I_{aS})]\,(\mathbf{R}) = \iiint \iiint g_{aS}(\mathbf{R},\mathbf{r}_1)|\chi^{(3)}_{aS}(\mathbf{r}_1)|^2 g_{aS}(\mathbf{R},\mathbf{r}_2)|\chi^{(3)}_{aS}(\mathbf{r}_2)|^2 g_S(\mathbf{r}_1-\mathbf{r}_2)\mathrm{d}\mathbf{r}_1\mathrm{d}\mathbf{r}_2, \tag{4}$$

where $g_s = |C_S|^2$ is the autocorrelation of the Stokes speckle intensity. Since $\mathcal{V}$ depends quadratically on $|\chi^{(3)}_{aS}|^2$, recovering the sample from the speckle-CARS image variance is a non-trivial operation. CARS-RIM uses an iterative reconstruction algorithm, algoRIM, that estimates $|\chi^{(3)}_{aS}|^2$ so as to minimize the distance between the empirical variance and its model, Eq. (4). AlgoRIM requires the knowledge of $g_{aS}$ and $g_S$ and is based on a fast calculation of Eq. (4), which is detailed in the supplementary information 1 part 2. In theory, algoRIM is able to recover the sample spatial frequencies over the Fourier support of $g^2_{aS}$, which corresponds to the resolution of an ideal confocal fluorescence microscope [15].

To begin RIM iterative inversion procedure, the initial estimate of the sample is set as the empirical standard deviation of the recorded speckle-CARS images. This simple data processing, named DSI-CARS, in reference to the Dynamic Speckle Illumination approach (DSI) in fluorescence microscopy [20] generally yields a better starting point than the average-CARS image. The optical sectioning arises in DSI because at the camera imaging plane the incoherent CARS speckle grains are in focus and the intensity for each camera pixel varies a lot for different speckle illuminations. On the contrary for out of focus camera imaging plane, the blurred CARS speckle grains generate poor camera pixel intensity variations for different speckle illuminations. Indeed, we observed that DSI-CARS provided optical sectioning, as illustrated in Fig. 1c and in the supplemental information 1 part 3.

## 3. Results

The axial and transverse resolutions of CARS-RIM reconstructions were first studied on synthetic data obtained with a CARS microscope simulator [19]. In Fig. 2b, a simulated sample is considered that is composed of an axially thin, homogeneous layer featuring a uniform transverse spatial density of $|\chi^{(3)}_{aS}|^2$. CARS-RIM and average-CARS reconstructions were obtained for different axial positions of the layer with respect to the detection focal plane, yielding a z-profile of the sample. As expected, the average-CARS profile is a constant whereas the CARS-RIM profile peaks when the thin layer is in focus. CARS-RIM axial resolution, given by the full width at half maximum (FWHM) of the latter was about $\approx$1.6µm, which is close to that of a confocal fluorescence microscope $1.4\lambda_{aS}/NA^2 = 1.78$µm [21]. Note that in this particular case, RIM iterative processing did not improve the z-profile given by the initial estimate, DSI-CARS, because the full axial resolution gain had already been achieved.

The transverse resolution of CARS-RIM is studied in Fig. 2c. We considered a thin inhomoge-

neous layer in which the scatterer concentration formed a star-like pattern in the transverse plane. CARS-RIM and average-CARS images were compared to the image provided by a coherent widefied CARS microscope using Stokes and pump collimated beam illumination (plane waves) propagating along the optical axis. As expected, we observe a significant improvement of the resolution from coherent CARS to average-CARS and from average-CARS to CARS-RIM.

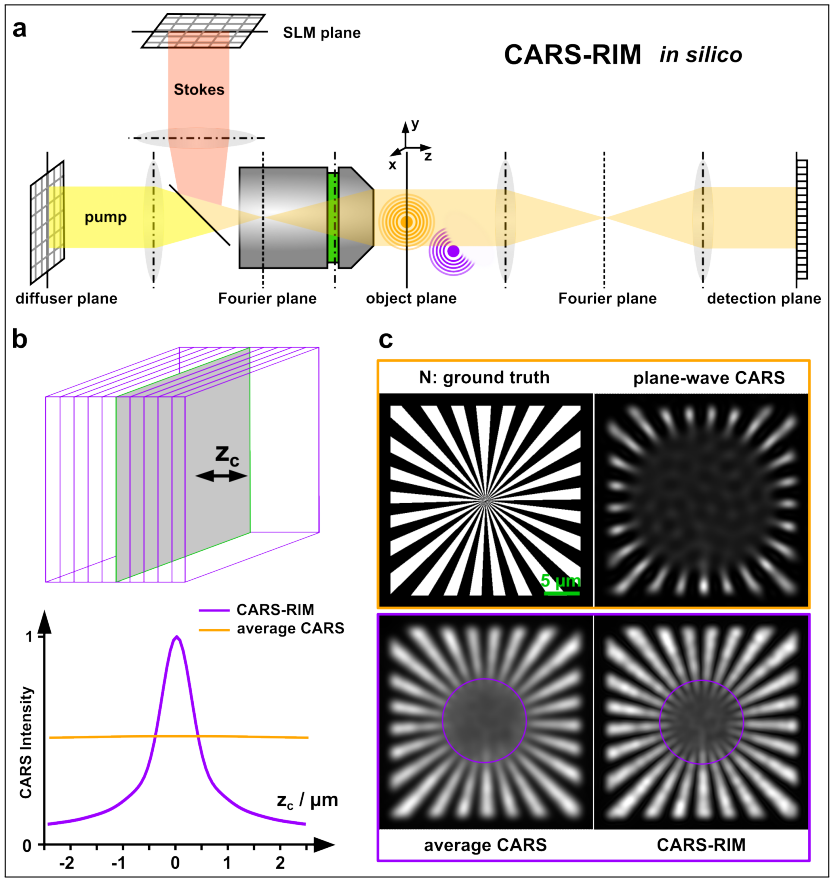


Fig. 2. CARS-RIM *in silico*: a) Schematic representation of the CARS-RIM microscope using a diffuser to generate the pump speckles and a spatial light modulator (SLM) to generate the Stokes speckles. The sample is imaged on the camera sensor in transmission. b) Study of the axial resolution of CARS-RIM with a single homogeneous thin layer that is scanned along the z optical axis. Speckled images are recorded for different positions $z_c$ of the layer with respect to the focal plane ($z_c = 0$). Average-CARS yields a constant intensity profile as a function of $z_c$ whereas CARS-RIM profile peaks when the layer is in focus. c) Study of the transverse resolution. Images of a thin layer featuring star-like inhomogeneous nonlinear scatterer density placed in-focus for different wide-field CARS imaging modalities (i) plane wave illumination, (ii) averaged-CARS (iii) and CARS-RIM. CARS-RIM resolution is better than that of average-CARS, which is superior to plane-wave CARS.

The analysis of the experimental performance of CARS-RIM was conducted on a home-made wide-field transmission microscope. A high-peak-power laser with a repetition rate of 515 kHz was used as the Stokes beam to drive the CARS four-wave-mixing process. The laser also pumped an optical parametric amplifier (OPA) to generate the color-tunable pump beam - see Fig. 3. The

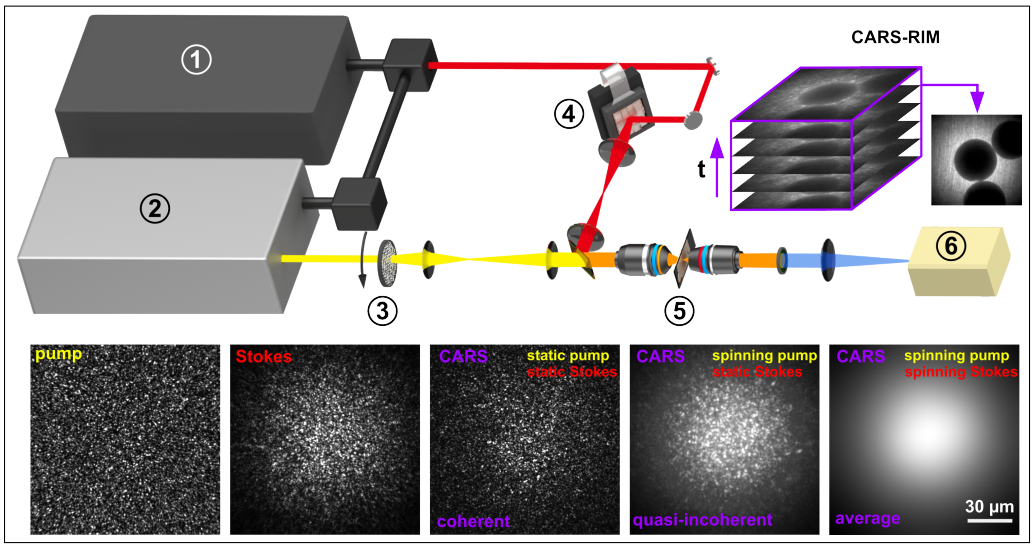


Fig. 3. Experimental setup: - 1 High peak-power laser, 2 optical parametric amplifier (OPA), 3 fast spinning diffuser, 4 spatial light modulator (SLM), 5 excitation and collections optics with the sample in between, 6 CMOS camera. Right top corner: stack of speckle-CARS images for different Stokes speckled illuminations and their CARS-RIM reconstruction. The lower part of the figure shows from left to right: a pump speckle; a Stokes speckle; CARS raw image of an olive oil thin film obtained with a static pump and static Stokes speckle illuminations at 2850 $cm^{-1}$ $CH_2$ symmetric stretching vibration; speckle-CARS image obtained by averaging the CARS raw images over a large number of pump speckles (keeping the Stokes speckles static); average-CARS image obtained by averaging the CARS raw images over a large number of pump *and* Stokes speckles.

Stokes speckled patterns were generated by a Spatial Light Modulator (SLM), while the pump speckles were formed through a rapidly spinning diffuser. Both the pump and Stokes beams passed through the same condenser to illuminate the sample. The anti-Stokes light was detected through a high-NA objective and was recorded with a camera placed at the image plane of a 4f imaging system. The speckle-CARS images were obtained by keeping the Stokes speckled beam static while averaging over the continuously varying pump speckles. The Stokes patterns were changed with the SLM every 50 ms (20 Hz). Supplementary video 1 shows raw live CARS (and SFG) images recorded by the camera with spinning pump speckle and 20Hz updating Stokes speckle. Note that this video is intended to exemplify the data acquisition to perform CARS-RIM (that require static Stokes speckle). Depending on the sample, the average-CARS or CARS-RIM images were reconstructed using 600 to 2000 CARS speckle images.

The axial resolution of CARS-RIM was studied using a thin film of olive oil sandwiched between two cover slips. The 3D image was obtained by translating the sample in steps of 1 µm along the axial direction. As expected, CARS-RIM was able to localize the oil film contrary to average-CARS, see Fig. 4a. The axial resolution of the reconstructed image stack, estimated from its spatial frequency cut-off along the axial spatial frequency direction, was approximately 3 µm. CARS-RIM 3D imaging was also tested on 30 µm diameter silica beads immersed in oil, see Fig. 4b and the supplementary video 2. The CARS-RIM images at different depths, Fig. 4b (left) are significantly crispier than that obtained with average-CARS. A set of CARS-RIM images taken by translating the sample along the optical axis was processed to recover the 3D shape of the spheres, Fig. 4b (right).

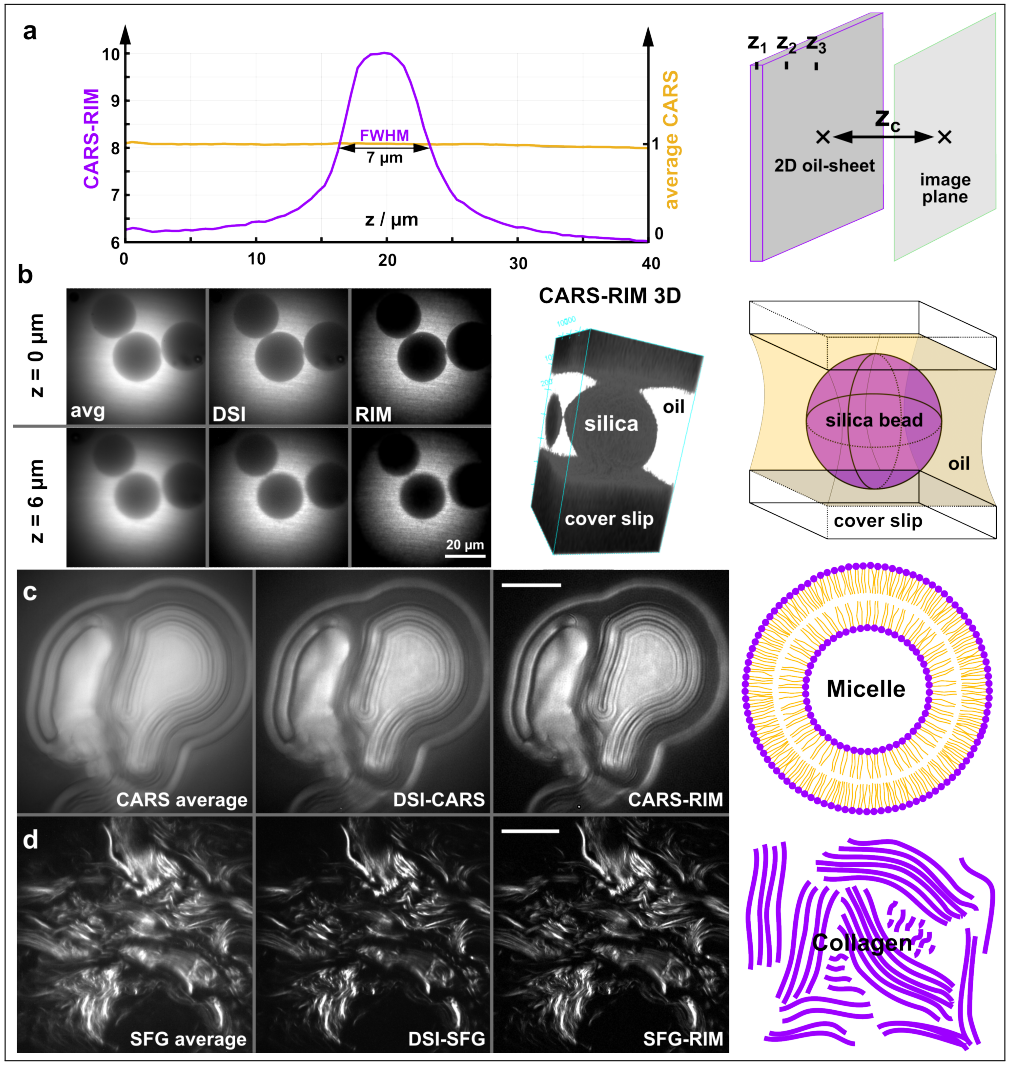


Fig. 4. Comparison between average-CARS, DSI-CARS, and CARS-RIM reconstructions of different samples represented schematically in the rightmost column. a) Average-CARS and CARS-RIM z-profiles of an approximately 5 µm thick sheet of olive oil sandwiched between 2 cover slips. The spatial frequency cut-off of the profile was found to be $\sim 1/3\ \mu m^{-1}$, yielding an axial resolution of about 3 microns. b) 30 µm diameter glass beads in olive oil imaged with CARS contrast at 2850 $cm^{-1}$ for two different depths (left) and CARS-RIM 3D reconstruction (right). The bead is clearly visible. c) Multi-lamellar vesicles imaged with CARS at 2850 $cm^{-1}$. d) Collagen tissue imaged with sum-frequency generation (SFG) contrast. In all cases, the CARS-RIM and SFG-RIM reconstructions are better resolved and better contrasted than average-CARS or DSI-CARS. The transverse resolution, was about 300 nm for the RIM images while an estimate of 650 nm was obtained for the average-CARS and -SFG images. In b), c) and d) are presented the average-CARS (or SFG) images, the standard deviation of the speckled images (DSI) and the RIM images. Average power in each beams ~250 mW. The white scale bar is 20 µm.

The resolution gain of CARS-RIM was further explored with samples showing more pronounced transverse spatial structure, such as multilamellar vesicles and human connective tissues, as shown in Fig.4c,d. Note that in Fig.4d, the CARS-RIM technique was applied to sum-frequency generation (SFG), this SFG contrast highlights the distribution of collagen in the sample. In the SFG case, the optical filter behind the collection objective lens is changed to detect the light at a frequency given by the sum of the pump and Stokes beam frequencies. The transverse resolution of CARS-RIM and SFG-RIM images in Fig. 4c,d were estimated with image cross sections (data not shown), to be 300 nm, while the resolution of average-CARS and average-SFG was estimated at about 650 nm. As expected there is a two-fold improvement of the resolution between average and RIM images.

The capability to excite both the CARS and SFG contrasts using the same experiment allowed us to acquire multi-modal images with both of these modalities. Fig. 5a shows a mosaic image of a 20 µm thick human breast tissue section covering the connective tissue and the epithelial layer down to the stratum corneum. For each image tile in the figure, 2000 speckle-CARS and speckle-SFG images were acquired sequentially. Clearly, CARS-RIM and SFG-RIM images exhibited better optical sectioning and transverse resolution than average-CARS and average-SFG.

Lastly, in Fig. 5b, we show that the resolution gain of CARS-RIM is compatible with spectroscopic applications. We imaged a mixture of a powder of polypropylene (PP) and 60 µm diameter polystyrene beads (PS) that were suspended in deuterated water ($D_2O$). Speckle-CARS images were acquired at the Raman resonance frequencies 2400 $cm^{-1}$, 2850 $cm^{-1}$ and 3050 $cm^{-1}$ matching the stretching vibrations of $D_2O$, the methylene groups (-$CH_2$-) within PP and the aromatic rings (=C-H) within PS, respectively. The CARS-RIM images nicely distinguished the different chemical bonds.

## 4. Discussion

Wide-field nonlinear microscopy is still in its infancy, but the advent of high power lasers oscillators and optical parametric amplifiers makes it a promising technique for imaging large samples with molecular specificity at high acquisition rates. Up to now, the few attempts to develop wide-field nonlinear imaging were plagued by plane wave illumination schemes leading to (i) low spatial resolution, (ii) the lack of optical sectioning, and (iii) experimental difficulties due to harmful beam focusing at the fragile back-focal plane of objective lenses. CARS-RIM and SFG-RIM have broken free of these limitations. Using speckled illuminations followed by statistical reconstruction, they provide images with (i) optical z sectioning and (ii) enhanced spatial resolution as compared to plane-wave non-linear imaging. In the supplementary information section 4 we show that for the same average power, a speckle wide-field illumination (with independent pump and Stokes speckles) generates $\sim 2$ times more CARS signal than a plane-wave illumination for thin samples. This is because the CARS signal generation in bright speckle grains overcompensates for dark speckle grains due to the cubic dependency of the CARS signal on the excitation fields. In addition, the speckle illumination scheme is harmless to the condenser and objective lenses and is extremely resilient to beam misalignment and optical or specimen aberrations. This is in sharp contrast with point scanning nonlinear microscopy that requires delicate beam alignment, spatial beam superposition and low-aberration numerical condenser objectives to activate the CARS and SFG contrasts. Furthermore, CARS-RIM reconstruction algorithm needs only the spatial frequency support of the condenser to estimate the sample, rather than the full complex pupil, including aberrations, that is required for widefield harmonic optical tomography or ptychography [19, 22].

CARS-RIM microscopy is based on a theoretical analysis showing that averaging the CARS signal over the pump speckles while keeping the Stokes speckled beam static can yield a speckle-CARS image similar to that obtained in Random Illumination fluorescence Microscopy (RIM), with $|\chi^3_{aS}|^2$ standing for the fluorescence density and the Stokes intensity standing for

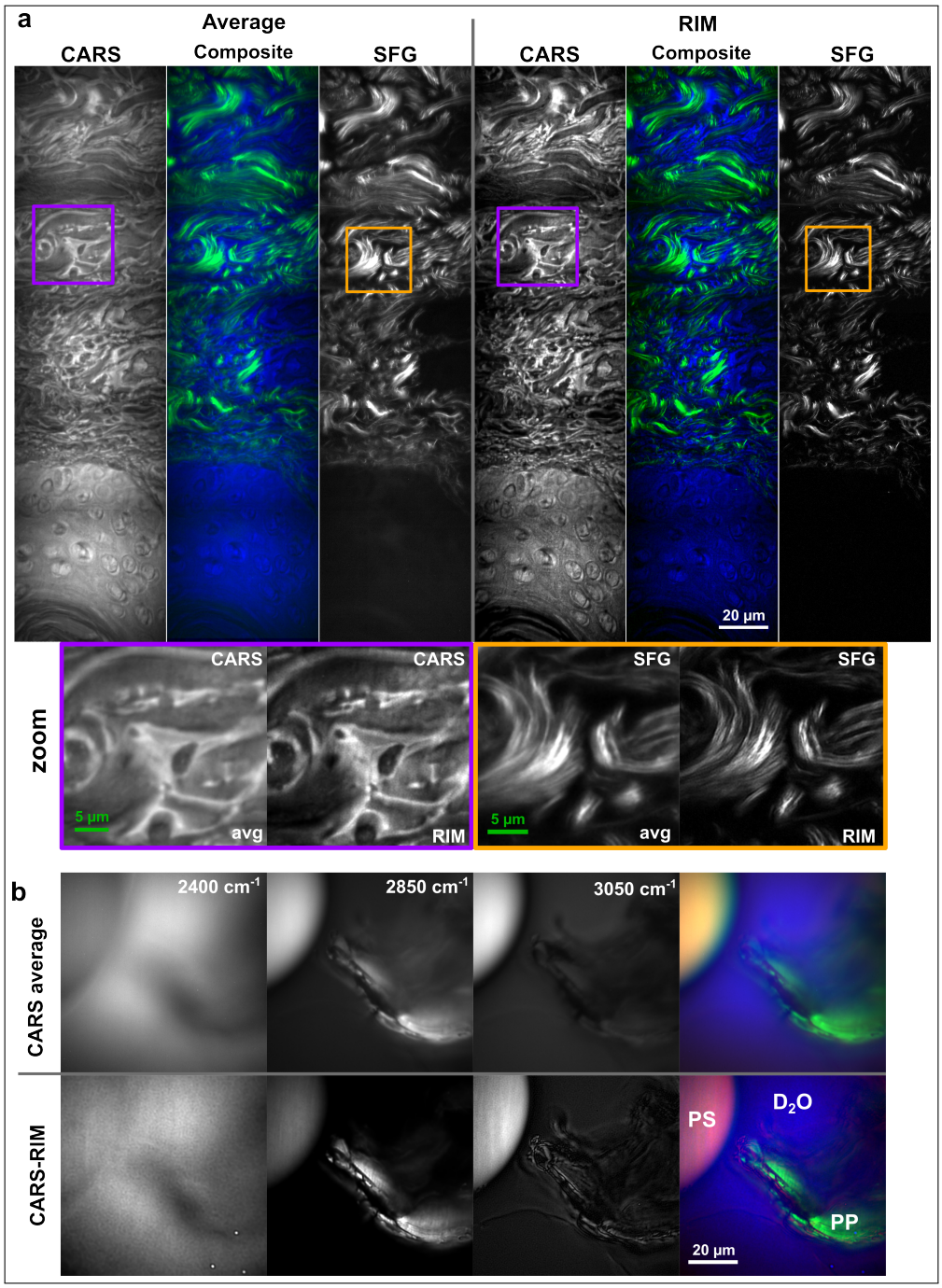


Fig. 5. a) Multimodal imaging of connective tissue of a 20 µm thick human skin sample. The CARS-RIM and SFG-RIM images (right column) are compared to average-CARS and average-SFG images. The composite image corresponds to the superposition of SFG and CARS signal. b) Spectroscopic CARS-RIM images of polystyrene beads in a suspension of polypropylene powder diluted in deuterated water. The CARS signal is detected at Raman resonances 2400cm$^{-1}$, 2850cm$^{-1}$ and 3050cm$^{-1}$ matching the stretching vibrations of deuterated water ($D_2O$), the methylene (-$CH_2$-) group within polypropylene (PP) and the aromatic =C-H breathing vibration of polystyrene (PS), respectively. Average power in each beams ~250 mW.

the speckled illumination [16]. The fluorescence-like model is valid for slowly varying samples or dispersed point-scatterers. It requires the Stokes speckle grains to be much larger than the pump grains (which is the case if the pump speckles are generated through an objective with a numerical aperture close to unity). CARS-RIM statistical data processing consists in forming the variance of multiple (600 to 2000) statistically independent speckle-CARS images obtained under different random Stokes speckled patterns. It is shown that the variance is a complex quadratic functional of $|\chi^3_{aS}|^2$, which depends on the Stokes speckle auto-correlation and the anti-Stokes point spread function. These two functions are usually well-known and can be computed or measured experimentally. The sample is then estimated iteratively by minimizing the distance between the experimental variance and the variance model. It was demonstrated that such data processing yields reconstructions that are linear to the sample with transverse resolution and optical sectioning comparable to that of a confocal microscope [14, 15]. In practice, CARS-RIM provided sample reconstructions with a resolution estimated to 3 µm axially and 0.3 µm laterally, Fig. (4). These results place CARS-RIM spatial resolution at the level of scanning CARS microscopy [2] with the advantage of a robust set-up requiring minimal control over the co-propagating pump and Stokes speckled beams.

In our experimental implementation, the field of view was about $80 \times 80$ µm$^2$ and the temporal resolution of CARS-RIM (using several hundred to thousands of speckled images) was about a few tens of seconds, this is two orders of magnitude slower than state-of-the-art scanning CARS. Yet, there is clear room for improvement. Faster SLMs and cameras could reduce the acquisition time per speckled image to 1ms (instead of the present 50 ms). In addition, one could reduce the number of speckle images per reconstruction to 50 at the cost of some granular artifacts in the reconstruction due to the residual inhomogeneity of the illumination on average [16]. Using complementary speckles [23] could help reduce these artifacts by forming a uniform illumination with only few speckles. We expect that combining kHz SLMs and cameras as well as fast signal processing would yield CARS-RIM images at a few frames per second.

Furthermore, we showed in the supplementary information section 4, that with our laser average power and repetition rate, widefield CARS-RIM requires theoretically $\sim 4$ times lower peak intensity density on the sample as compared to point scanning CARS (for equal total CARS signal and equal acquisition time) leading to fewer toxic multi-photon absorption events. Interestingly, we show that it is possible to adjust the laser parameters (average power and repetition rate) of wide-field CARS to perform faster image acquisition than in point scanning (for equal peak-intensity density), or to diminish the peak-intensity density (and the heating) for an equal image acquisition time than in point scanning (see supplementary information sections 4 and 5). This versatility is not possible in point scanning CARS where the acquisition time and the peak-intensity density (and its induced phototoxicity) cannot be dissociated. Finally, whereas only 1/3 of the pump and Stokes speckle grains overlap with pump and Stokes independent speckles, we show that this leads to $\sim 2$ times more CARS signal than using plane wave illumination (see supplementary information section 4).

CARS-RIM principle works for any two-color nonlinear process. In this work, it was applied to CARS and non-degenerate three-wave mixing (SFG) imaging. Still, it could also be readily extended to four-wave mixing processes such as non-degenerate third harmonic generation. We obtained multimodal images of human skin samples where collagen (SFG signal), nuclei and borders of epithelial cells (CARS signal) were clearly distinguished, Fig. (5)a. We believe these multi-modal images could be diagnostically relevant [24, 25] and useful for medical applications. In another experiment, the spectroscopic ability of CARS-RIM combined with its confocal axial resolution permitted to distinguish beads embedded in a powder suspension, Fig. (5b), paving the way towards three-dimensional spectroscopic analysis of materials in a wide-field scheme. Implemented with the spectral focusing scheme [26, 27] CARS-RIM could address a narrower vibrational band and generate hyper-spectral images with reduced non-resonant background

contribution [28] enabling its potential for *in vivo* applications in biology and medical sciences.


## Acknowledgements

The authors thank Paulina Gasecka for the preparation of the lipid multilamellar vesicle sample and Romain Appay for providing the human tissue sections. The authors also thank Light Conversion for providing the PHAROS laser and the ORPHEUS-HP optical parametric amplifier.


## Author contributions

E.M.F prepared the samples and performed the experiments. S.H. conceived the idea, assisted the experiments and performed the numerical calculations. S. L. developed the RIM reconstruction algorithm, algoRIM. D.G. assisted the experiments and installed the laser source. A.S. conceived the idea and derived the analytical description of CARS-RIM with the help of R.B. H.R. conceived and supervised the project. S.H. A.S. H.R. R.B wrote the manuscript. All authors discussed the results and commented on the manuscript.

## Competing financial interests

The authors declare no conflict of interest.


## Funding Information

We acknowledge financial support from the Centre National de la Recherche Scientifique (CNRS), A*Midex (ANR-11-IDEX-0001-02), ANR grants (ANR-10-INSB-04-01, ANR-11-INSB-0006, ANR-16-CONV-0001, ANR-21-ESRS-0002 IDEC), INSERM 22CP139-00. This has received funding from European Union's Horizon 2020 (EU ICT 101016923 CRIMSON and Marie Skłodowska-Curie Actions ITN 812992 MUSIQ) and European Research Council (ERC, SpeckleCARS, 101052911). Views and opinions expressed are however those of the author(s) only and do not necessarily reflect those of the European Union or the European Research Council. Neither the European Union nor the granting authority can be held responsible for them.


## References


1. P. D. Maker and R. W. Terhune, "Study of optical effects due to an induced polarization third order in the electric field strength," Phys. Rev. **137**, A801–A818 (1965).
2. A. Zumbusch, G. R. Holtom, and X. S. Xie, "Three-Dimensional Vibrational Imaging by Coherent Anti-Stokes Raman Scattering," Phys. Rev. Lett. **82**, 4142–4145 (1999).
3. H. Rigneault and P. Berto, "Tutorial: Coherent raman light matter interaction processes," APL Photonics **3**, 091101 (2018).
4. J.-X. Cheng and X. S. Xie, eds., *Coherent Raman Scattering Microscopy (Series in Cellular and Clinical Imaging)* (CRC Press, 2016).
5. C. L. Evans, E. O. Potma, M. Puoris'haag, D. Cote, C. P. Lin, and X. S. Xie, "Chemical imaging of tissue in vivo with video-rate coherent anti-stokes raman scattering microscopy," PNAS **102**, 16807–16812 (2005).
6. H. Wang, Y. Fu, P. Zickmund, R. Shi, and J.-X. Cheng, "Coherent anti-stokes raman scattering imaging of axonal myelin in live spinal tissues," Biophys. J. **89**, 581–591 (2005).
7. S. Yue and J.-X. Cheng, "Deciphering single cell metabolism by coherent raman scattering microscopy," Curr. Opin. Chem. Biol. **33**, 46–57 (2016).
8. M. T. Cicerone and C. H. Camp, "Histological coherent raman imaging: a prognostic review," The Analyst **143**, 33–59 (2018).
9. Y. Fu, H. Wang, R. Shi, and J.-X. Cheng, "Characterization of photodamage in coherent anti-stokes raman scattering microscopy," Opt. Express **14**, 3942 (2006).
10. C. Heinrich, S. Bernet, and M. Ritsch-Marte, "Wide-field coherent anti-stokes raman scattering microscopy," Appl. Phys. Lett. **84**, 816–818 (2004).
11. I. Toytman, K. Cohn, T. Smith, D. Simanovskii, and D. Palanker, "Wide-field coherent anti-stokes raman scattering microscopy with non-phase-matching illumination," Opt. Lett. **32**, 1941 (2007).
12. P. Berto, D. Gachet, P. Bon, S. Monneret, and H. Rigneault, "Wide-field vibrational phase imaging," Phys. Rev. Lett. **109** (2012).

13. P. Berto, A. Jesacher, C. Roider, S. Monneret, H. Rigneault, and M. Ritsch-Marte, "Wide-field vibrational phase imaging in an extremely folded box-CARS geometry," Opt. Lett. **38**, 709 (2013).
14. J. Idier, S. Labouesse, M. Allain, P. Liu, S. Bourguignon, and A. Sentenac, "On the superresolution capacity of imagers using unknown speckle illuminations," IEEE Transactions on Comput. Imaging **4**, 87–98 (2018).
15. S. Labouesse, J. Idier, A. Sentenac, M. Allain, and T. Mangeat, "Proof of the resolution-doubling of random illumination microscopy using the variance of the speckled images," in *2021 29th European Signal Processing Conference (EUSIPCO),* (2021), pp. 1159–1162.
16. T. Mangeat, S. Labouesse, M. Allain, A. Negash, E. Martin, A. Guénolé, R. Poincloux, C. Estibal, A. Bouissou, S. Cantaloube, E. Vega, T. Li, C. Rouvière, S. Allart, D. Keller, V. Debarnot, X. B. Wang, G. Michaux, M. Pinot, R. L. Borgne, S. Tournier, M. Suzanne, J. Idier, and A. Sentenac, "Super-resolved live-cell imaging using random illumination microscopy," Cell Reports Methods **1**, 100009 (2021).
17. C. Heinrich, A. Hofer, S. Bernet, and M. Ritsch-Marte, "Coherent anti-stokes raman scattering microscopy with dynamic speckle illumination," New J. Phys. **10**, 023029 (2008).
18. J. W. Goodman, *Speckle phenomena in optics: theory and applications* (Roberts and Company Publishers, 2007).
19. S. Heuke, K. Unger, S. Khadir, K. Belkebir, P. C. Chaumet, H. Rigneault, and A. Sentenac, "Coherent anti-stokes raman fourier ptychography," Opt. Express (2019).
20. C. Ventalon and J. Mertz, "Quasi-confocal fluorescence sectioning with dynamic speckle illumination," Opt. Lett. **30**, 3350 (2005).
21. L. Novotny and B. Hecht, "Preface," in *Principles of Nano-Optics,* (Cambridge University Press, 2006), pp. xv–xviii.
22. C. Hu, J. J. Field, V. Kelkar, B. Chiang, K. Wernsing, K. C. Toussaint, R. A. Bartels, and G. Popescu, "Harmonic optical tomography of nonlinear structures," Nat. Photonics **14**, 564–569 (2020).
23. J. Gateau, H. Rigneault, and M. Guillon, "Complementary speckle patterns: Deterministic interchange of intrinsic vortices and maxima through scattering media," Phys. Rev. Lett. **118**, 043903 (2017).
24. A. Medyukhina, T. Meyer, S. Heuke, N. Vogler, B. Dietzek, and J. Popp, "Automated seeding-based nuclei segmentation in nonlinear optical microscopy," Appl. Opt. **52**, 6979 (2013).
25. S. Heuke, N. Vogler, T. Meyer, D. Akimov, F. Kluschke, H.-J. Röwert-Huber, J. Lademann, B. Dietzek, and J. Popp, "Multimodal mapping of human skin," Br. J. Dermatol. **169**, 794–803 (2013).
26. E. Gershgoren, R. A. Bartels, J. T. Fourkas, R. Tobey, M. M. Murnane, and H. C. Kapteyn, "Simplified setup for high-resolution spectroscopy that uses ultrashort pulses," Opt. Lett. **28**, 361 (2003).
27. T. Hellerer, A. M. Enejder, and A. Zumbusch, "Spectral focusing: High spectral resolution spectroscopy with broad-bandwidth laser pulses," Appl. Phys. Lett. **85**, 25–27 (2004).
28. J.-X. Cheng and X. S. Xie, "Coherent anti-stokes raman scattering microscopy: instrumentation, theory, and applications," The J. Phys. Chem. B **108**, 827–840 (2003).
29. F. Szoka and D. Papahadjopoulos, "Comparative properties and methods of preparation of lipid vesicles (liposomes)," Annu. Rev. Biophys. Bioeng. **9**, 467–508 (1980).

## Methods

### *4.1. Numerical Simulations*

All the simulations of the CARS-RIM experiments were performed by calculating Eq. (1) and using the image formation technique described in [19]. For simplicity, we approximated the anti-Stokes susceptibility tensor by $\chi^{(3)}_{aS} \approx \chi^{(3)}_{aS,1111}$, implying that we only considered x-polarized light in excitation and detection. The pump and Stokes speckled beams were generated using two independent masks placed at a conjugated image plane with random phases which were uniformly distributed in $[0,2\pi]$ and random amplitude in [0,1]. Each wide-field speckle-CARS image was obtained through the averaging over 800 distinct pump speckle patterns for one fixed Stokes pattern. Then, 400 speckle-CARS images were generated for 400 different Stokes speckle patterns. The numerical aperture (NA) of the excitation and detection objectives were set to 0.9 and the Stokes, pump and antiStokes wavelengths to $1030nm$, $800nm$ and $654nm$, matching our experimental conditions.

### *4.2. CARS-RIM reconstruction procedure*

All the CARS-RIM super-resolved images were obtained with the reconstruction code algoRIM which is accessible at https://github.com/teamRIM/tutoRIM. The different steps of the reconstruction procedures are detailed in the supplementary information 1 part 2. AlgoRIM requires the knowledge of diffraction-limited $g_{aS}$ and $g_S$ with the experimental parameters $NA_S$, $\lambda_S$ and

$NA_{aS}$. The tuning of Tikhonov parameters required by algoRIM for dealing with the signal to noise ratio of the speckled images was performed manually.

### 4.3. Experimental setup

The CARS-RIM setup is shown schematically in Fig. 3. The output of a Yb-based amplified solid-state laser (Light Conversion, PHAROS; 150 fs, 20 W, 515 kHz, 1030 nm) is split into 2 parts. Part 1 serves as the Stokes beam to drive the CARS four-wave mixing process. The second part is coupled into an optical parametric amplifier (OPA; Light Conversion, ORPHEUS-HP) whose emission at 650 – 900 nm is used as the pump beam for the CARS generation. The pump beam goes through the outer edge of a 2" diameter fast-spinning (≈5Hz) optical diffuser (Thorlabs, DG20-220). The Stokes beam is centered onto a spatial light modulator (SLM, BNS, HSPDM256-700-900) and recombined as well as temporally superimposed with the pump pulses using a dichroic mirror (Thorlabs, DMSP900L) and a mechanical delay stage. The illuminated spots at the diffuser and SLM are imaged by a 10x telescope (Thorlabs LA1509-B-ML; Nikon, MBL71105, effective NA 0.9 under water immersion) onto the sample. The power at the sample was approximately 250mW per color dispersed over a field of view larger than 80µm. To obtain 3D images, the sample is moved along the optical axis using a motorized translation stage (PI, M-110.12S). Speckle CARS radiation is collected in forward direction by a 40x objective lens (Nikon, PLAN, NA = 1.15, immersion: water), separated from the excitation wavelength by dielectric filters (Thorlabs, FESH0700) and imaged by a second tube lens (Thorlabs, AC254-200-B-ML) onto a CMOS camera (Hamamatsu, ORCA-fusion, C14440). A Matlab-based control software is used to switch between random phase-mask pattern of the SLM which is synchronized to the trigger of the camera's readout.

### 4.4. Sample preparation

Preparation of the glass beads in oil: glass beads (diameter 30µm, ThermoFisher) were deposited on a standard glass object older (thickness 1mm) and a droplet of oil (IMMOIL-F30CC, Olympus) was added. The sample was sealed using a standard coverslip (thickness 170µm) but no spacer was used to avoid floating of the beads along the direction of gravity.

Preparation of the lipid vesicles: The multilamellar vesicles were prepared following the instructions outlined in [29]. Briefly, the lipids (dissolved organic carbon (DOC), Avanti Polar Lipids) are dissolved in chloroform within a beaker creating a 10mM solution. The organic solvent is slowly evaporate using a stream of dry nitrogen. The resulting layer of lipids at the bottom of the beaker is suspended in cyclohexane. Dry ice is added to freeze the mixture of lipids and cyclohexane. The solidified mixture is placed under high vacuum to remove the cyclohexane. Multilamellar vesicles are obtained by dissolving the remnant lipids in an aqueous buffer (Phosphate Buffered Saline, Sigma-Aldrich) for 30-60 minutes at room temperature.

Preparation of the multi-component sample: polystyrene beads (diameter 60 µm, Fluka Analytical) and polypropylene (PP, Sigma-Aldrich) powder were mixed and placed on a glass object holder. To match the refractive index and immobilize the sample, the mixture of powders were immersed in a solution of 1% of agarose (thermoscientific, TopVision Agarose) in deuterium oxide (Sigma-Aldrich, deuteration degree min. 99.9%). A 100 µm thick spacer and a standard coverslip has been used to seal the sample.

Preparation of the tissue sample: 20 µm thick unstained tissue sections from a surgery of a human breast were provided by the public bio-bank hospital of La Timone hospital (Marseille, FR). A droplet of de-ionized water was added on top of the tissue matching its refractive index in order to reduce linear scattering of the sample. To avoid draining of the water and a potential contamination of the condenser lens, the tissue sample was sealed using a 100 µm thick spacer and a cover slip.

## Data Availability

The data that support the findings of this study are available from the corresponding authors upon request.